SUPPLEMENTAL MATERIAL

Oxidative Stress Creates a Unique, CaMKII Mediated Substrate for Atrial Fibrillation in Heart Failure

Shin Yoo, Gary Aistrup, Yohannes Shiferaw, Jason Ng, Peter J. Mohler, Thomas J. Hund, Trent Waugh, Suzanne Browne, Georg Gussak, Mehul Gilani, Bradley P Knight, Rod Passman, Jeffrey J. Goldberger, J Andrew Wasserstrom, and Rishi Arora

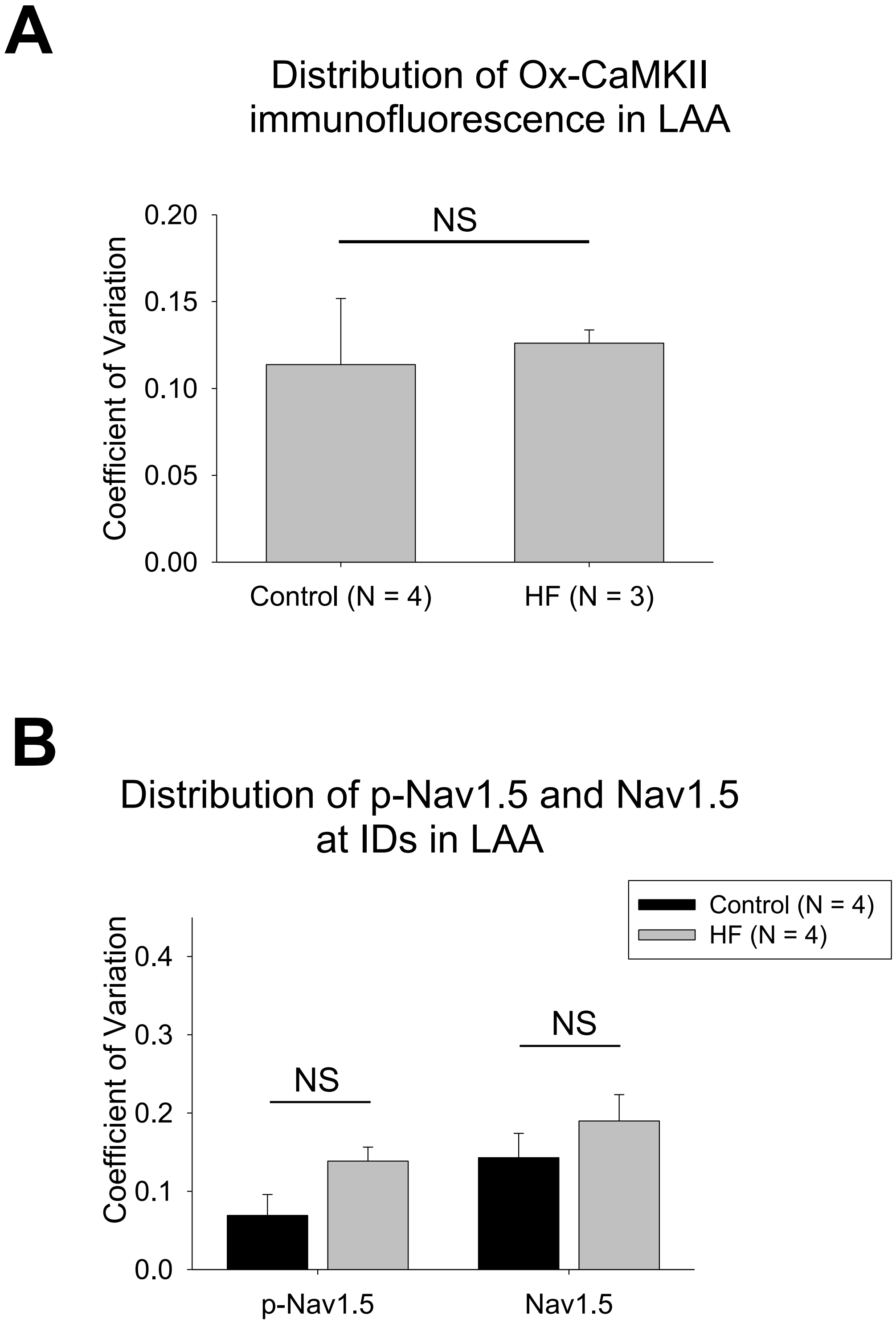

Supplemental figure S1. Spatial distribution of Ox-CaMKII, and CaMKII-p-Na$_v$1.5 (S571) and Na$_v$1.5 in control and HF LAA. (A and B) No significant difference in spatial distribution of Ox-CaMKII (A) and CaMKII-p-Na$_v$1.5 (S571) and Na$_v$1.5 (B) in control and HF LAA. Data are represented as Mean ± SEM. NS, not significant vs. control using unpaired t-test.

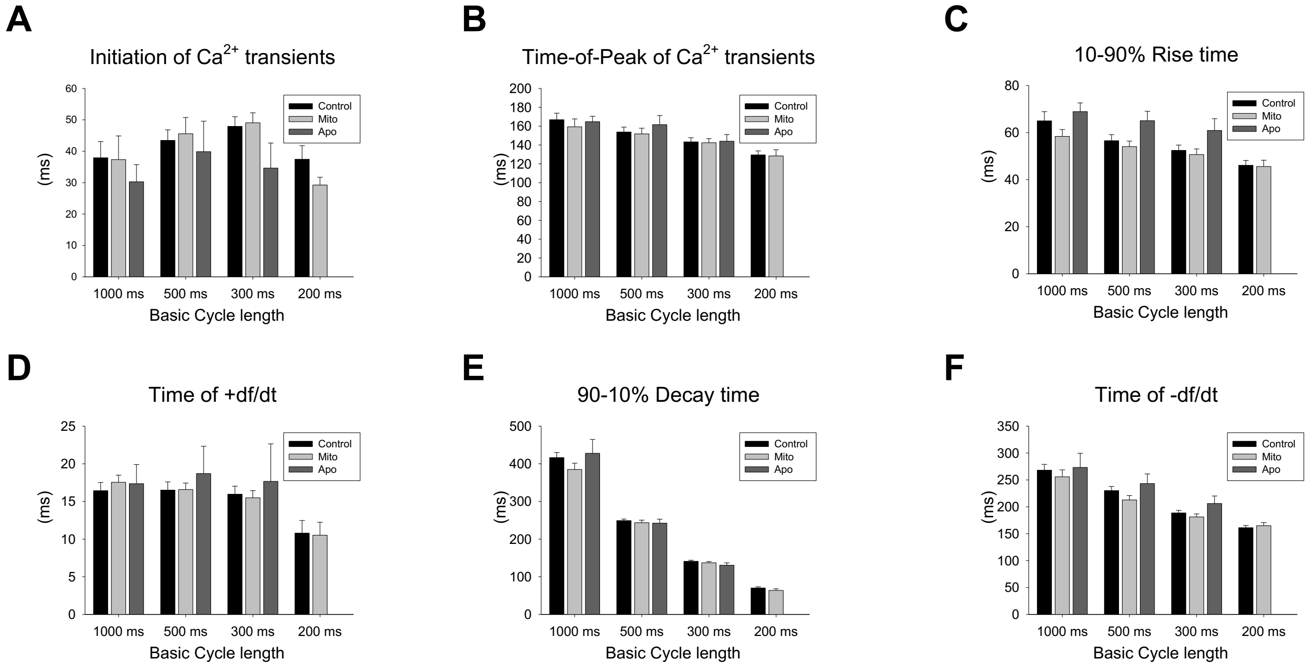

Supplemental figure S2. Results of Ca^{2+} transients analysis (1). (A) initiation of Ca^{2+} transients (B) Time of peak of Ca^{2+} transients (C) 10 - 90 % rise time (D) Time of +df/dt (E) 90 - 10% decay time (F) Time of – df/dt. Data are represented as Mean ± SEM. Not significant vs. control using unpaired t-test.

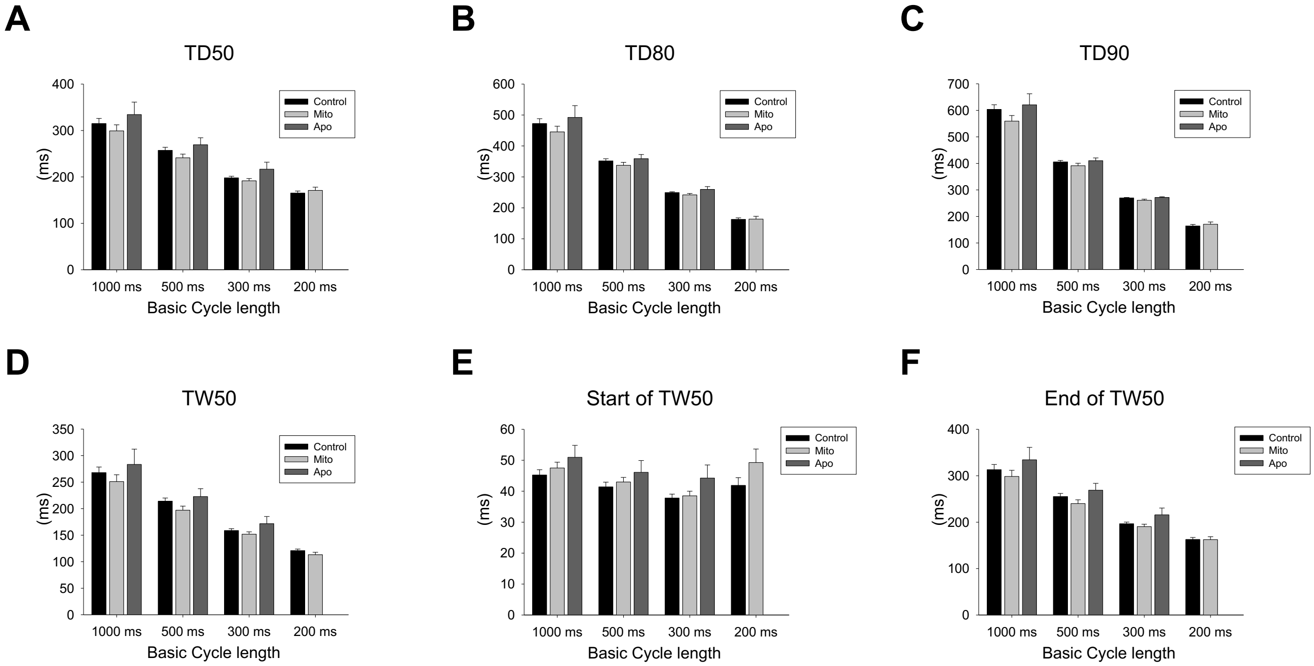

Supplemental figure S3. Results of Ca^{2+} transients analysis (2). (A) TD50 (B) TD80 (C) TD90 (D) TW50 (E) Start of TW50 (F) End of TW50. Data are represented as Mean ± SEM. Not significant vs. control using unpaired t-test.

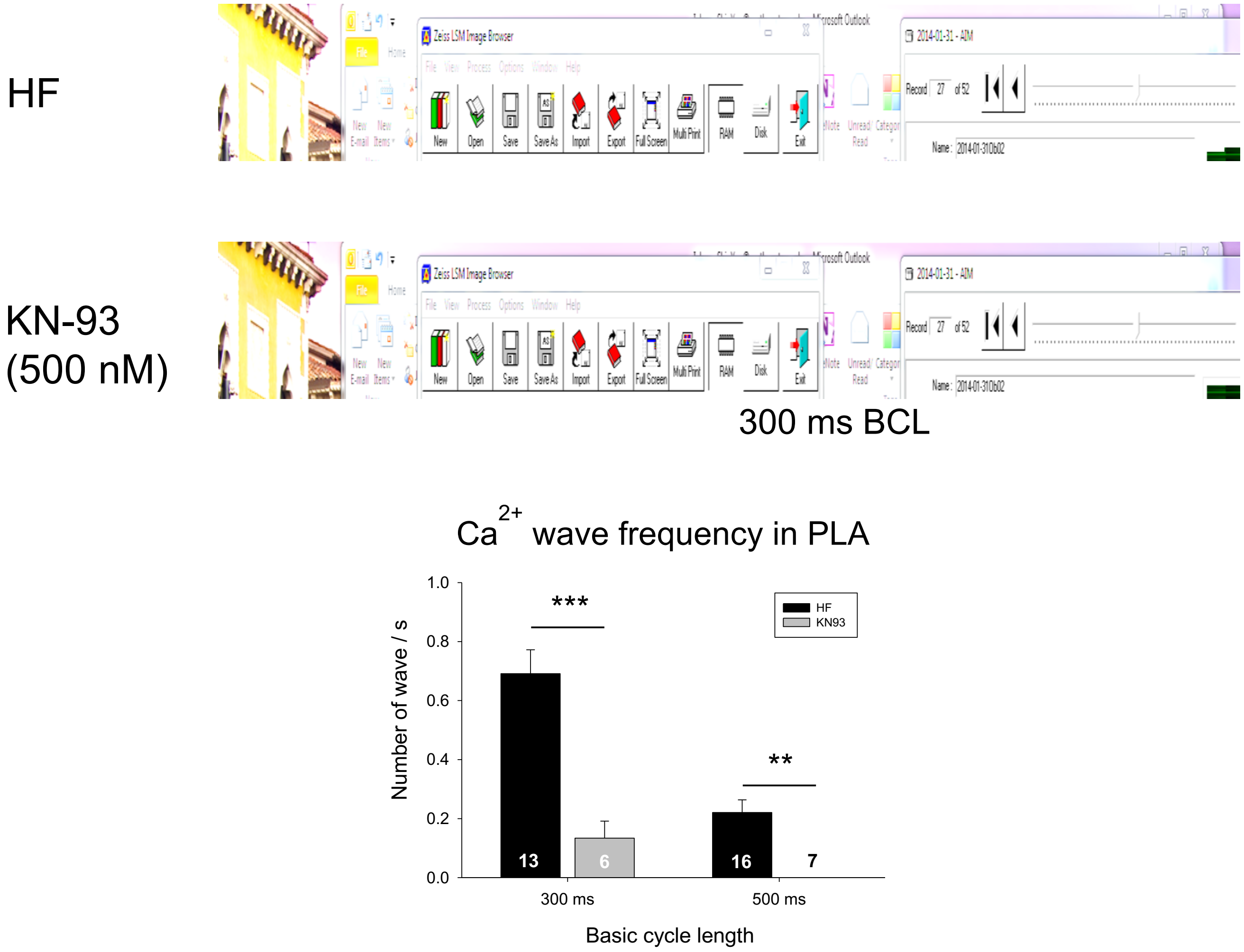

Supplemental figure S4. Attenuation of TCW by application of a CaMKII inhibitor, KN93. Attenuation of incidence of TCW at 500 ms and 300 ms BCL by application of KN93 in HF PLA myocytes. Time bar, 1 s. Data are represented as Mean ± SEM. ** $P < 0.01$, *** $P < 0.001$ unpaired t-test.

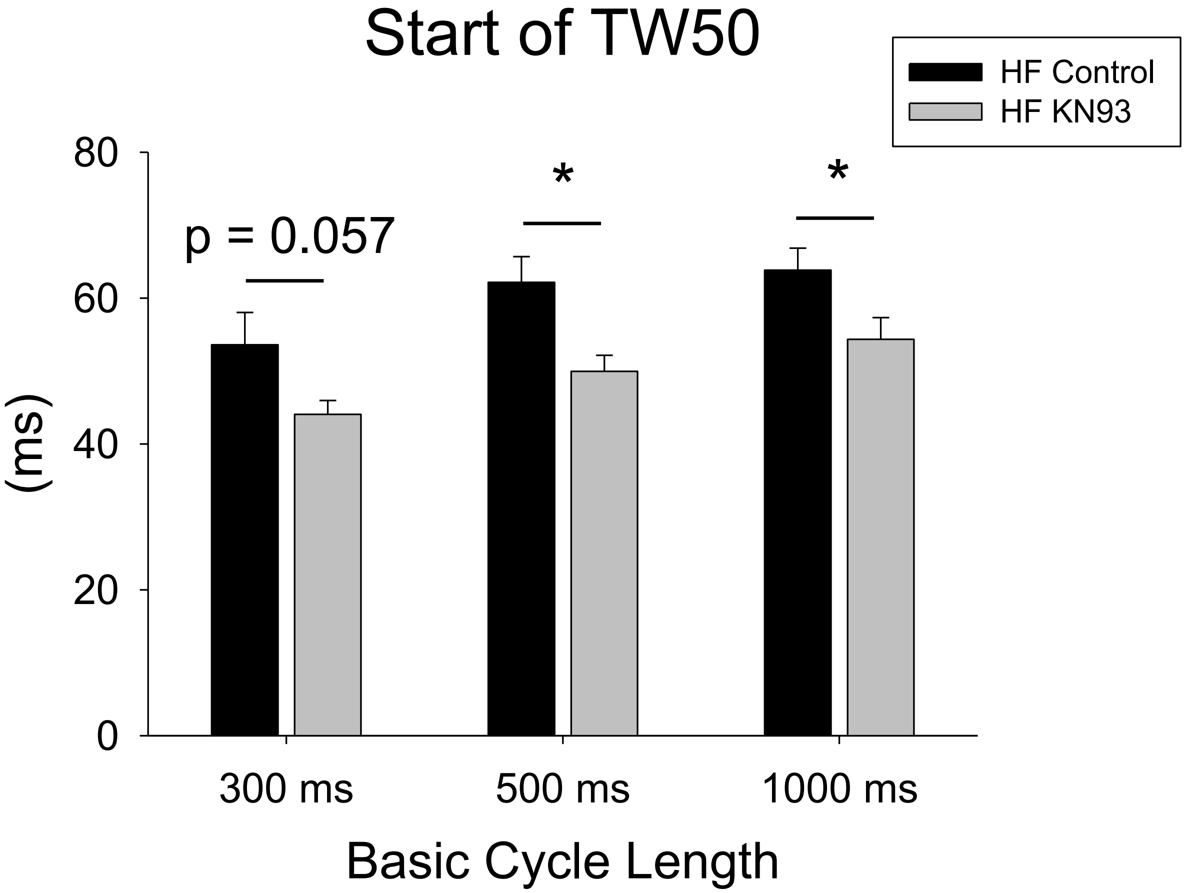

Supplemental figure S5. Change of start of TW50 in the presence of KN93 in HF PLA atrial myocytes.

Data are represented as Mean ± SEM. * $P < 0.05$, unpaired t-test.

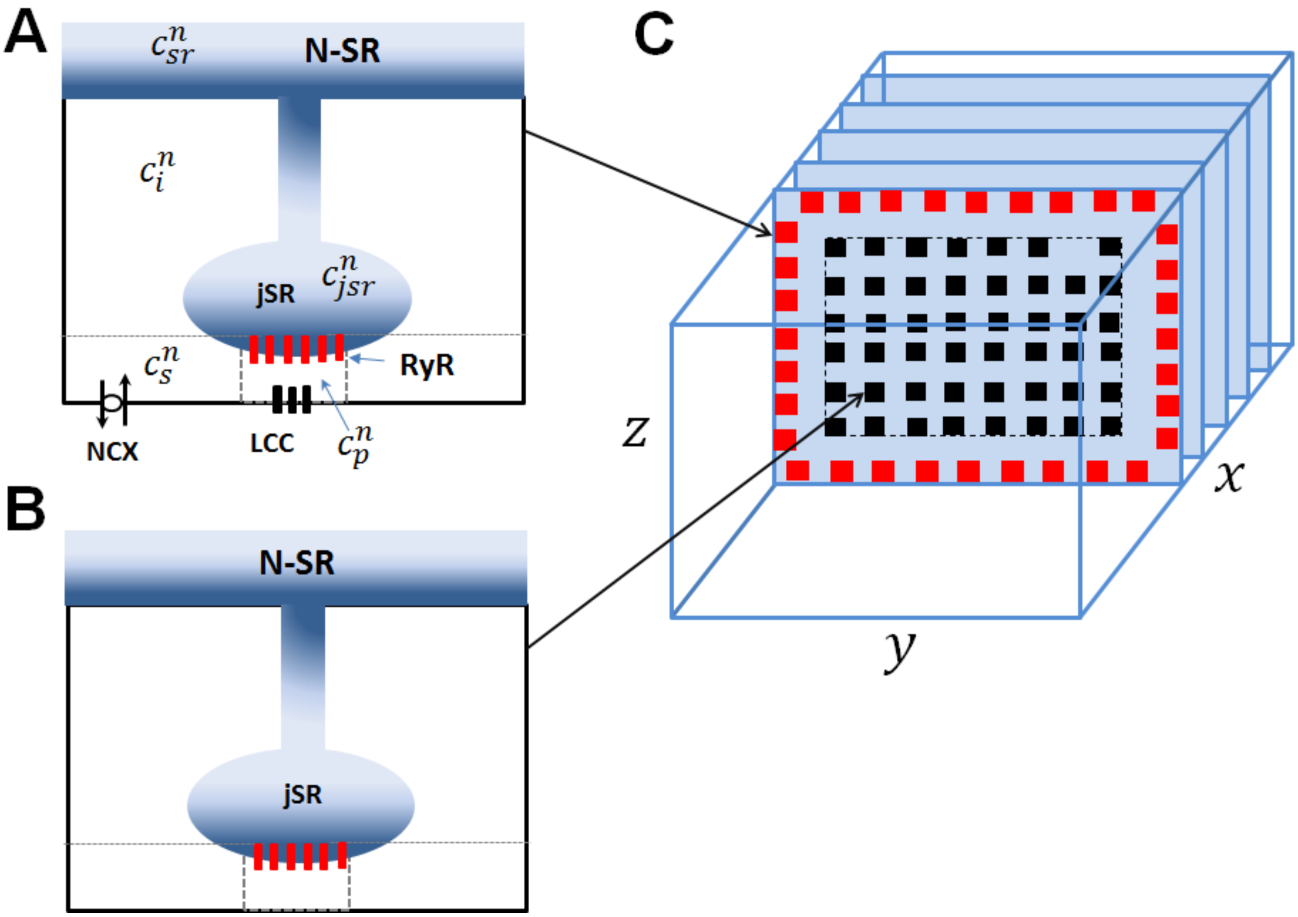

Supplemental figure S6. Mathematical model of atrial myocytes. Schematic illustration of the spatial architecture of Ca signaling in a cardiac ventricular cell. Ca signaling and release occurs within dyadic junctions distributed in the 3D volume of the cell. Dyadic junctions close to the cell membrane (A) possess LCC and NCX channels, while interior junctions (B) do not have these channels. Here, the superscript n denotes the n^{th} dyadic junction in a 3D grid representing the cell. (C) Spatial architecture of the cell interior showing Z-planes. All compartments in the other boundary are treated as junctional CRUs (red squares).

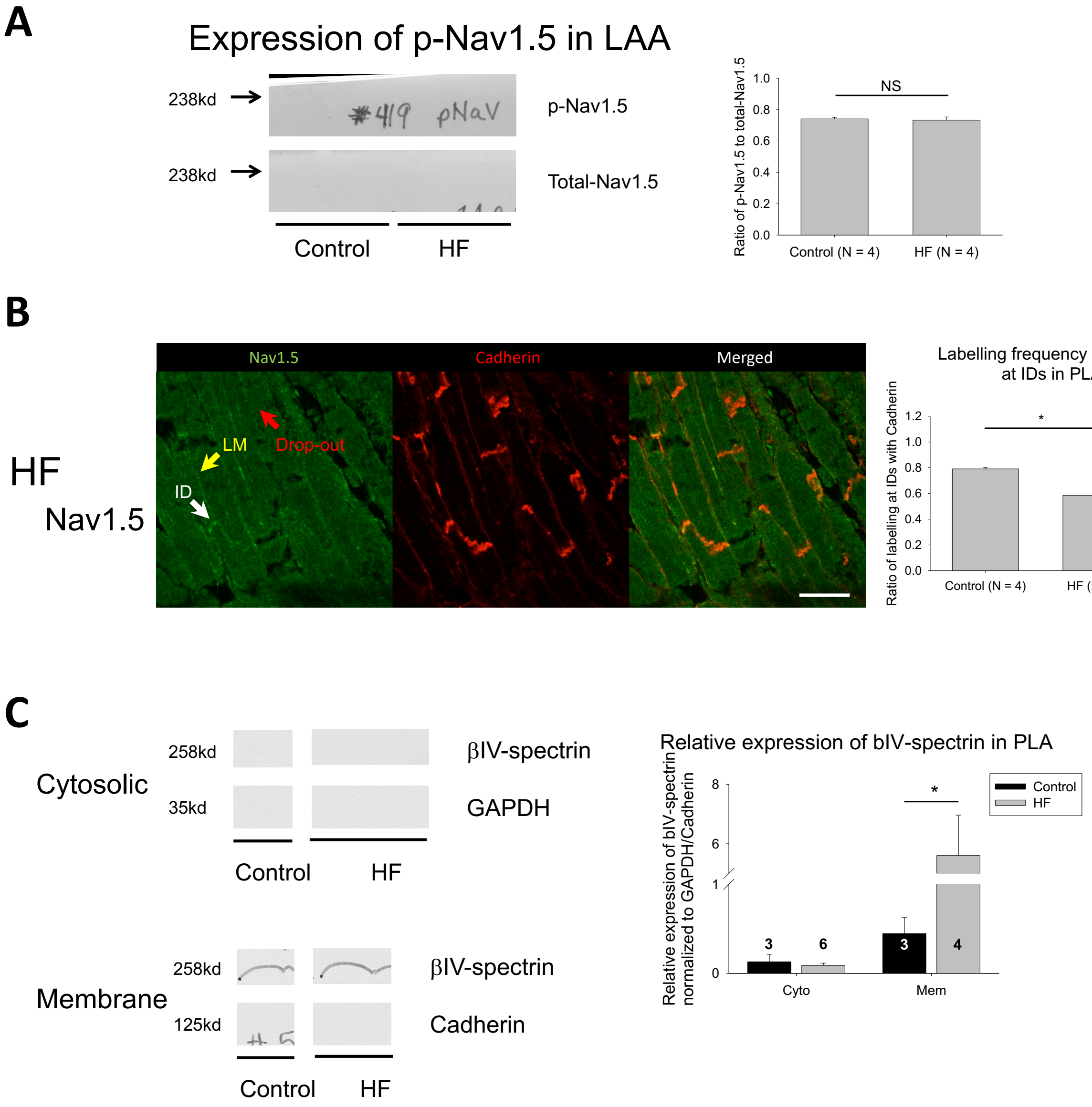

Supplemental figure S7. Drop-out of Na$_v$1.5 at ID in HF PLA and expression of βIV-spectrin in cytosolic and membrane fractions of control and HF PLA. (A) Representative western blot and densitometric measurements of CaMKII-p-Na$_v$1.5 (S571) (normalized to native Na$_v$1.5) from control and HF in LAA. (B) (left panel) While Na$_v$1.5 was still localized at the lateral membrane (LM, yellow arrows) in HF PLA, there was a drop-out of Na$_v$1.5 at certain ID (red arrow), where cadherin labelling was still intact at those ID. (right panel) Quantification of myocytes with relative ID labelling of Na$_v$1.5 with cadherin in control and HF PLA. Scale bar, 40 μm. (C) Representative immunoblot and densitometric measurements of βIV-spectrin (normalized to GAPDH and Cadherin) in cytosolic and membrane fractions from control and HF PLA. Data are represented as Mean ± SEM. * $P < 0.05$, unpaired t-test.

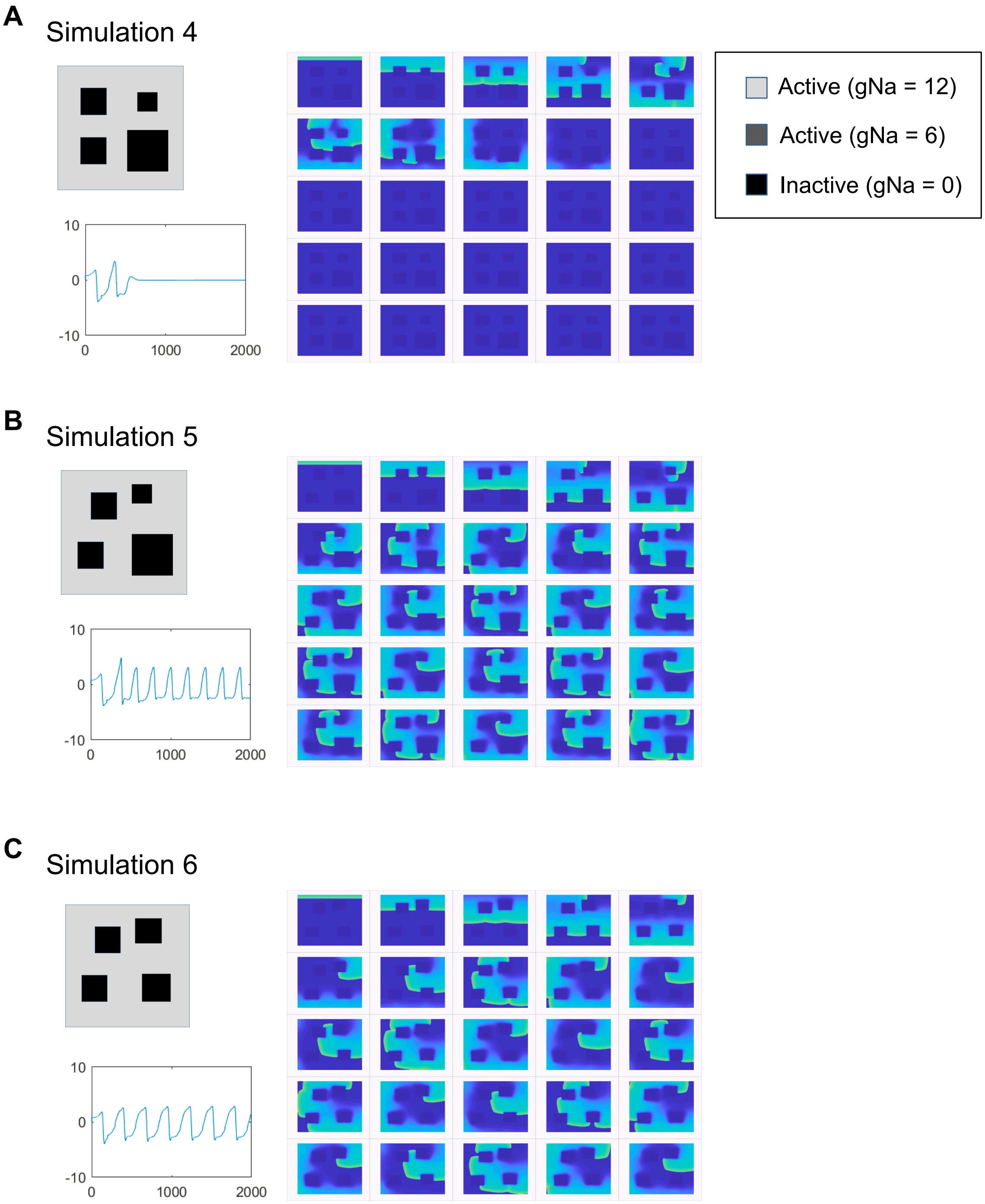

Supplemental figure S8. Mathematical simulation of action potential propagation in 2D atrial tissue containg different configuration of fibrosis. Simulations were performed in 2D atrial tissue with same dimension as described in main manuscript (Figure 9). Arrhythmia induction was performed in 3 different fibrosis configurations: (A) fibrosis with different size, but homogeneous distribution; (B) fibrosis with different size and heterogeneous distribution; (C) fibrosis with same size, but heterogeneous distribution. In each condition, 25 screen shots of activation movie were taken every 75 ms.

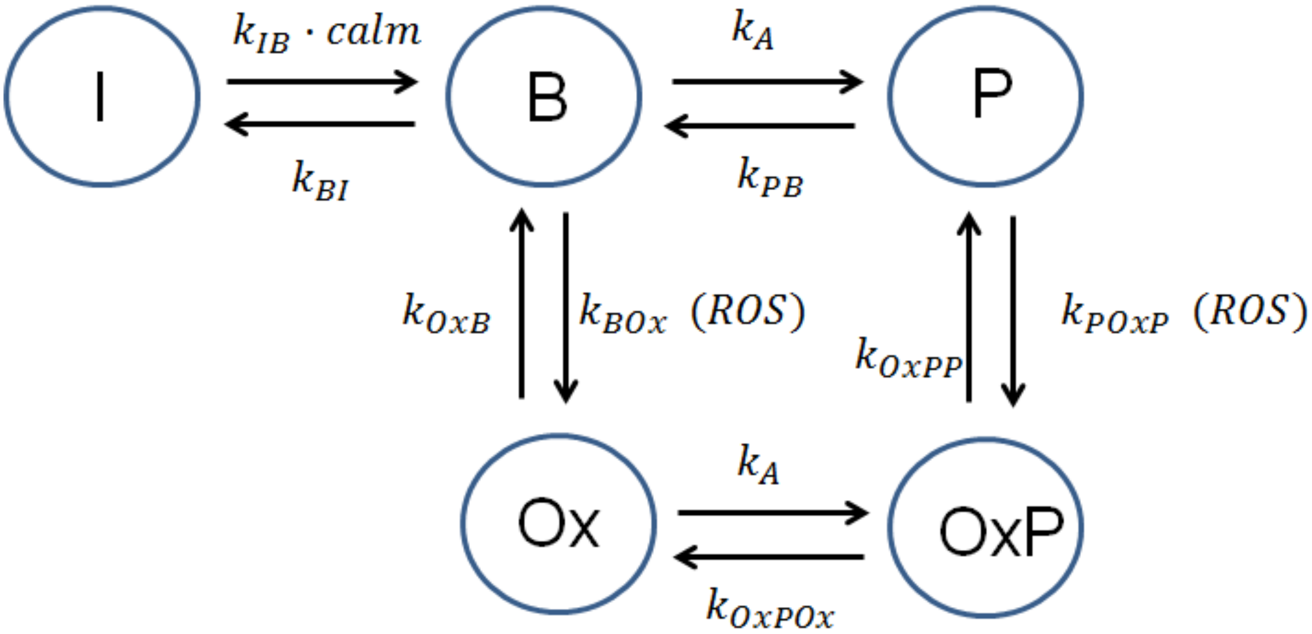

Supplemental figure S9. The state diagram of CaMKII activation by oxidation.

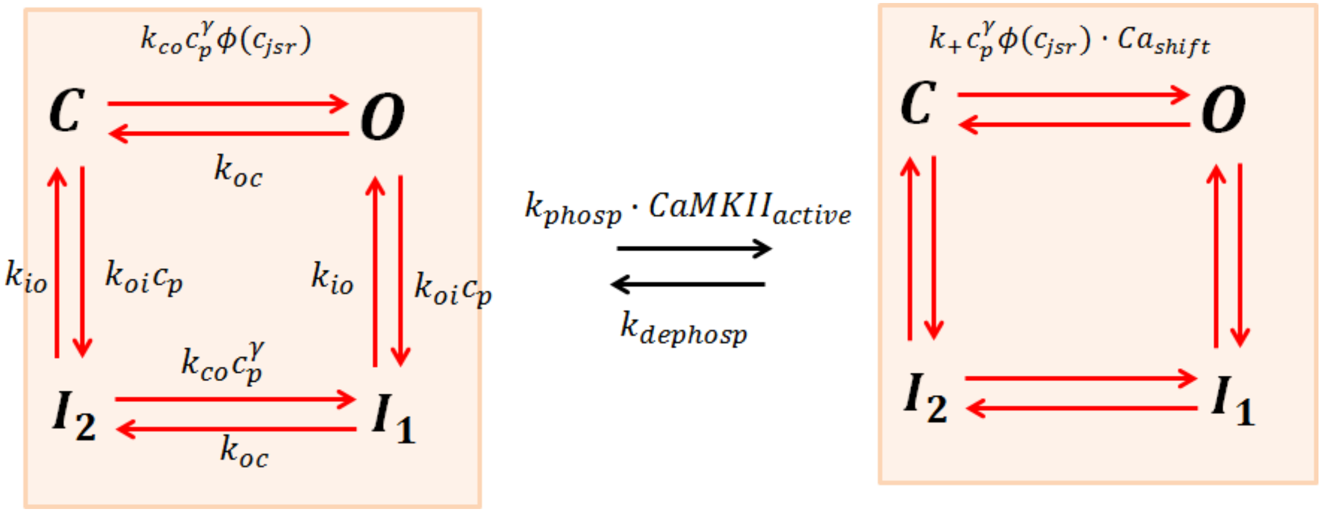

Supplemental figure S10. Markov state model of RyR. Four states on the left correspond to the unphosphorylated states of the channel, and the right corresponds to phosphorylated states. Transitions rates between phosphorylated and unphosforylated states are CaMKII dependent.

SUPPLEMENTAL RESULTS

Ca^{2+} transient analysis

As described in the main manuscript, ROS is upregulated in the canine HF left atrium and preferentially increased in the HF PLA. This is accompanied by higher expression of Ox-CaMKII and increased CaMKII phosphorylation of RyR2 in the HF PLA (Figures 2A, and 3A). We therefore performed Ca^{2+} imaging experiments to assess Ca^{2+} handling in the presence of mitochondrial ROS scavenger, mito-TEMPO and a NOX2 inhibitor, apocynin. Besides attenuation of triggered Ca^{2+} waves (TCW) by mito-TEMPO (Figure 3C), we also examined the spatio-temporal properties of Ca^{2+} transients i.e., Rel. Peak Amplitude, Time of Peak, 10 - 90 % Rise-time, +dF/dt, -dF/dt, TD50, TD80, TD90, TW50. These were not significantly different between untreated vs. mitoTEMPO- or apocynin-treated myocytes (Supplemental figures S3 and S4).

We performed similar Ca^{2+} imaging experiments and Ca^{2+} transient analysis in the presence of a CaMKII inhibitor, KN93. The only statistically significant difference in Ca^{2+} transient properties between control and KN93 in HF atrial myocytes was start of TW50, not TW50 (Supplemental figure S5). This parameter means shift of start time of spatial spread; since the amount of spatial spread (TW50) was still the same, a change in the start of TW50 is of unclear functional significance.

DETAILED METHODS

HF model development

Purpose-bred hound dogs (weight range: 25-35 kg; age range: 1-3 years) used in this study were maintained in accordance to the Guide for the Care and Use of Laboratory Animals published by the U.S. National Institutes of Health (NIH Publication No. 85-23, revised 1996) as approved by the IACUC of the Northwestern University. Before undergoing the procedures listed below, all animals were premedicated with acepromazine (0.01 – 0.02 mg/kg) and were induced with propofol (3-7 mg/kg). All experiments were performed under general anesthesia (inhaled) with isoflurane (1-3 %). Adequacy of anesthesia was assessed by toe pinch and palpebral reflex. Canine HF model was induced by right ventricular tachypacing (240 beats/min) for 3 weeks.

In-vivo EP study

For *in-vivo* EP study, high density electrical mapping was performed using the UNEMAP mapping system (Univ. of Auckland, Auckland, New Zealand). A triangular plaque containing 130 electrodes (inter-electrode distance of 2.5 mm) was used to record 117 bipolar EGMs at a 1 kHz sampling rate. Electrograms were obtained at normal sinus rhythm (NSR), 400 ms, 300 ms and 200 ms cycle length at baseline and after 3 weeks of pacing.

Data analysis for conduction velocity and conduction inhomogeneity

Electrograms were recorded at NSR, 400 ms, 300 ms and 200 ms cycle length at baseline and after 3 weeks of pacing using the UNEMAP mapping system. MATLAB (Mathworks, Natick, MA) was used for all offline signal analysis in this study and the bipolar electrograms were high-pass filtered at 30 Hz, rectified, and then low-pass filtered at 20 Hz. The times of the filtering peaks were considered the activation time for that activation. Then, the conduction velocity was calculated from the gradients of the activation times and the conduction inhomogeneity analysis was calculated by activation time difference, i.e. range of the phase differences, as previously described by Lammers et al (1).

Assessment of superoxide generation

Frozen tissue samples were crushed and rotor homogenized with protease inhibitor (Halt protease and phosphatase inhibitor cocktail, Thermo-Scientific). Protein concentrations were determined using Pierce BCA Protein Assay Kit (Thermo-Scientific). Lucigenin (5 µmol/L, Enzo Life Sciences) and NADPH (100 µmol/L, Calbiochem) were each added in the presence and absence of the following inhibitors: apocynin (NADPH oxidase(NOX2)), mito-TEMPO (mitochondrial reactive oxygen species (ROS) scavenger), L-NMMA (nitric oxide synthase) and oxypurinol (xanthine oxidase). The photon outputs were measured using a luminometer (Berthold Technologies, LUMAT LB 9507).

Assessment of protein carbonylation

The oxidation status of atrial tissue was determined by following the recommended protocol for the Oxiselect Protein Carbonyl Immunoblot Kit (Cell Biolabs, Inc. - Cat # STA-308). First, a standard SDS-PAGE electrophoresis gel was run and transferred to a PVDF membrane. The membrane was then immersed in a dinitrophenylhydrazine (DNPH) solution for the derivatization of the carbonyl group followed by incubations with the anti-DNP primary antibody and secondary antibody that were supplied with the kit. The immunoblot was developed on film using standard chemiluminescence techniques and the band densities were analyzed using ImagJ.

Immunoblot

Total protein extracts were extracted from snap-frozen canine atria by using the lysis buffer containing 20 mM Tris-HCl (pH 8.0), 100 mM NaCl, 1 mM EDTA, 0.5 % NP-40 and 1 x protease inhibitor cocktail solution. Protein concentrations were determined using Pierce BCA Protein Assay Kit (Thermo-Scientific) and BSA was used as a standard. Total protein extracts of 20-30 µg were separated on 10 % SDS-PAGE gels, and transferred to polyvinylidene difluoride membranes (Immun-Blot PVDF Membrane, BioRad). The membranes were incubated with 5 % nonfat dry milk in PBST (phosphate-buffered saline (PBS), 0.05 % (v/v) Tween-20 (Sigma), pH 7.4), and then probed with the primary antibody and horseradish peroxidase-conjugated secondary antibodies. The protein signal was visualized by using the ECL detection system (Amersham Biosciences). The membranes were re-probed using anti-cadherin or GAPDH antibodies, which serves as the loading control. All results were scanned and quantified by ImageJ.

Cryosectioning and Immunohistochemistry

Canine atrial tissue was excised and PLA, midPLA, and LAA regions were dissected. The preparations were frozen in OCT tissue freezing medium (VWR) at ~-50 ºC in 2-methyl butane cooled by dry ice, and stored at -80°C until use. The frozen preparations were secured on the chuck of a cryostat with tissue-freezing medium and serially sectioned (at - 25 °C) at 10 µm thickness. Sections were mounted on Superfrost Plus slides (VWR) and stored at - 80 °C until use.

Sections taken from -80 ºC freezer were undergone fixation with 4 % PFA, and washed 3 times in PBS. The sections were then permeabilized by incubating them in PBS containing 0.1 Triton X-100 (Sigma) for 10 min. After washing three times in PBS, the sections were blocked in 10 % normal goat serum (NGS; Sigma) in PBS for 1 hr. The sections were incubated with primary antibodies diluted with PBS containing 1 % Bovine Serum Albumin (BSA; Sigma) and 10 % NDS in a humid box at -4 °C overnight. The sections were washed three times in PBS, and incubated with secondary antibodies diluted with same solution as primary antibodies in a humid box at RT in the dark for 1 hr. After washing three times in PBS, the sections were mounted with Dapi containing mounting media (Vector Labs) and sealed with nail polish. Labelling was visualised using an epi-fluorescent microscope (Axiovision observer, Zeiss) or laser scanning confocal microscope (Zeiss LSM510 META). Aquired images were analyzed by LSM examiner, axiovision, Zen2012, and image J.

Data analysis for immunohistochemistry

Heterogeneity of distribution of ox-CAMKII in any single section was assessed by calculating the coefficient of variation of the immunofluorescence intensity for each of nine, randomly selected panels (10x magnification). Coefficient of variation of ox-CAMKII intensity was then compared between HF and control samples (for PLA and LAA), using unpaired t-tests. The heterogeneity of distribution of CaMKII-p-Nav1.5 (S571) in the atrium was assessed by quantifying the ratio of CaMKII-p-Nav1.5 (S571) labelling at the ID against cadherin labelling at the ID in a random sample of nine images. Coefficient of variation of CaMKII-p-Nav1.5 (S571) was then compared between HF and control samples (for PLA and LAA), using unpaired t-tests.

Isolation of single atrial myocytes

While the dog was still deeply anesthetized, the hearts was quickly removed and immersed in cold cardioplegia solution containing (mM) NaCl 128, KCl 15, HEPES 10, $MgSO_4$ 1.2, NaH_2PO_4 0.6, $CaCl_2$ 1, glucose 10, and heparin (0.001 U/mL); pH 7.4. All solutions were equilibrated with 100% O_2. The aorta was cannulated, and the heart was perfused with cold cardioplegia solution until effluent was clear of blood and heart was cold (5-10 min). The ventricles were cut away, the left circumflex coronary artery was cannulated, and the left atrium (LA) was dissected free. The left atrium was slowly perfused with cold cardioplegia while leaks from arterial branches were ligated with suture to assure adequate perfusion. The LA was then perfused with Tyrode's at 37 °C for 5 min to remove cardioplegia solution and assess for viability—i.e., the reestablishment of beating. If viable, the LA was then perfused at ~12 mL/min with Ca^{2+}-free Tyrode's solution for ~20 min, followed by ~40 min of perfusion with the same solution containing Liberase (Liberase TH Research Grade, Roche

05401151001) and 1% BSA; all at 37°C. Thereafter, the LA tissue was transferred to dish and cut into small pieces (~0.5 cm^2). These tissue pieces were then transferred to conical plastic tubes, and fresh enzyme solution (37 °C) was added. The tissue pieces were triturated in the fresh enzyme solution for 5-15 min for 15 min. The triturated tissue suspension was then filtered through nylon mesh (800 μm). The filtered cell tissue suspension was briefly centrifuged at ~500 g, then enzyme solution poured off, and cell tissue suspension resuspended in Tyrode's solution containing 200 μM Ca^{2+} and 0.1 % BSA. This resuspension was then and filtered through a nylon mesh (210 μm) was then and filtered through < 500 g, and again resuspended in Tyrode's solution containing 200 μM Ca^{2+} and 0.1% BSA to isolate dispersed cells. After cells settled for about 30 minutes, the solution was suctioned off and gradually replaced with a HEPES-buffered solution containing (mM) NaCl 137, KCl 5.4, $MgC1_2$ 1.0, $CaCl_2$ 1.8, HEPES 10, glucose 11, and 0.1% BSA; pH 7.4. After isolating the cardiomyocytes and raising the Ca^{2+} to 1.8 mM in 1X Tyrodes Solution.

Immunocytochemistry

The isolated atrial myocytes were placed on coverslips and washed with PBS (Phosphate Buffered Saline, pH 7.4, Sigma) and were fixed either in 10 % neutral buffered formalin (Sigma) for 15 min. The cells were then washed three times with PBS. The cells were permeabilized by incubating them in PBS containing 0.1 Triton X-100 (BDH) for 10 min. After washing three times with PBS, the cells were blocked in 10 % normal goat serum (NGS; Sigma) in PBS for 1 hour. The cells were incubated with primary antibodies diluted with PBS containing 1 % BSA and 10 % NDS in a humid box at -4 °C overnight. After washing three times with PBS, the myocytes were incubated with secondary antibodies diluted with same solution as primary antibodies in a humid box at room temperature in the dark for 1 h. After washing three times with PBS, the myocytes were mounted with Vectashield mounting media (Vector Labs) and sealed with nail polish. Labelling in isolated atrial myocytes was visualized using confocal microscope (Zeiss LSM510 META).

Antibodies

Primary antibodies: (1) rabbit polyclonal anti-oxidized CaMKII (Ox-CaMKII; GeneTex); (2) rabbit polyclonal anti-CaMKII (Genetex); (3) rabbit polyclonal anti-phospho-cardiac sodium channels at serine 571 (CaMKII-p-Na_v1.5 (S571)) (gift from Dr. Mohler); (4) rabbit polyclonal anti-Na_v1.5 (gift from Dr. Mohler); (5) rabbit polyclonal anti-phospho-RyR2 at serine 2814 (CaMKII-p-RyR2 (S2814)) (gift from Dr. Wehrens) (6) rabbit polyclonal anti-RyR2 (Thermo-fisher) (7) mouse monoclonal AnkG (gift from Dr. Mohler) (8) mouse monoclonal anti-cadherin (Abcam). Secondary antibodies: (1) goat anti-rabbit IgG conjugated to Alexa 488 (Invitrogen); (2) goat anti-mouse IgG conjugated to Alexa 568 (Invitrogen); (3) anti-mouse IgG conjugated HRP (Jackson Immunoresearch); (4) anti-rabbit IgG conjugated HRP (Jackson Immunoresearch).

Confocal Ca^{2+} imaging

Isolated PLA and LAA atrial myocytes were pre-incubated in various agents including apocynin, which inhibits NOX2, mito-TEMPO, a mitochondrial ROS scavenger and KN93, an inhibitor for CaMKII, longer than 2 hrs at room temperature. All the myocytes were incubated for ~20 min with 0.1% pluronic acid

(20 % stock in dimethlysufoxide) + 15 µM of Fluo-4AM (TEFLabs; 1mM stocks in dimethylsulfoxide) and an aliquot of Fluo-4AM loaded myocytes were then placed in recording chamber with electrical field stimulation. Intracellular Ca^{2+} cycling in field-stimulated myocytes was recorded as X-t linescans using Zeiss LSM-510 META confocal microscope. Stimulation protocols comprised of basal stimulation at a basic cycle length (BCL) of 1000 ms, 500 ms, 300 ms and 200 ms for 10-15 s per each rapid pacing epoch. Linescan images were analyzed using Zeiss LSM Examiner, MatLab and ImageJ software.

Mathematical modelling of Ca^{2+} dynamics

Atrial myocytes model: To model the spatiotemporal distribution of Ca^{2+} in atrial myocytes, we have implemented an established mathematical ventricular myocytes model by Restrepo et al (2, 3) (Restrepo model). In a recent study, we have used this model to explore the spatiotemporal dynamics of subcellular Ca^{2+} waves in atrial myocytes (4, 5). In this model, the cell interior was divided into an array of compartments that represent distinct intracellular spaces. The Ca^{2+} concentration within these compartments was treated as spatially uniform, and neighboring compartments were diffusively coupled. To model the atrial cell architecture, we first distinguished compartments that were close to the cell membrane, where L-type Ca^{2+} channels (LCC) and RyR channels occupied the same dyadic junction, and compartments away from the cell membrane which did not sense Ca^{2+} entry due to LCCs. For convenience we referred to compartments near the membrane as "junctional" Ca^{2+} release units (CRUs), and all other compartments as "non-junctional" CRUs. To model each compartment we denoted the Ca^{2+} concentration in compartment α as c_{α}^{n}, where the superscript n indicates the location of that compartment in a 3D grid representation of the cell interior. In this study we labelled our units according to the scheme $n=(n_x,n_y,n_z)$ where n_x denote the longtitudinal direction, n_y is the width of the cell, and n_z is the height. In Supplemental figures S6A and S6B, we show an illustration of the various compartments that comprise a junctional and non-junctional Ca^{2+} release unit (CRU) near the cell membrane. The intracellular compartments described in the model are: (1) The proximal space with concentration c_p^n and volume v_p. This compartment represents the volume of the cell that is in the immediate vicinity of the local RyR cluster. For junctional CRUs this space includes 1 - 5 LCC channels along with a cluster of 100 RyR channels, while for non-junctional CRUs, there are no LCC channels in the compartment. For junctional CRUs we follow the Restrepo model and take v_p to be the volume between the Junctional sarcoplasmic reticulum (SR) and the cell membrane, which is roughly a pillbox of height $10nm$ and diameter $100\ nm$. (2) The submembrane space, with concentration c_s^n and volume v_s, which represents a volume of space in the vicinity of the proximal space, but smaller than the local bulk myoplasm. For junctional CRUs we follow the Restrepo model and take v_s to be 5% of the cytosolic volume within a CRU. This volume includes Na^{+}-Ca^{2+} exchanger (NCX) which are regulated by Ca^{2+} concentrations that vary much faster than the average Ca^{2+} concentration in the myoplasm. (3) The bulk myoplasm, with concentration c_i^n and volume v_i, which characterizes the volume of space into which Ca^{2+} diffuses before being pumped back into the SR via the Sarcoplasmic Reticulum Ca^{2+} ATPase (SERCA, cardiac form SERCA2a) transporter. (4) The junctional SR (JSR), with concentration c_{jsr}^n, which is a section of the SR network in which the RyR channels are embedded. (5) The network SR (N-SR), with concentration c_{n-sr}^n, which represents the bulk SR network that is spatially distributed in the cell. In order to mimic the heterogeneity that is expected in a cardiac cell, we have also included spatial variation in the density of ion channels and transporters. In particular, if a CRU is designated as a junctional CRU then the probability that we insert NCX and LCC channels is taken to be 60%.

Our cardiac atrial myocytes model consists of 60 planes representing Z-planes, where each plane contains an array of 20×20 regularly spaced compartments (Supplemental figure S6C). All sites at the boundary of the cell are designated as junctional CRUs. Ca^{2+} diffusion between sites is modelled by allowing a diffusive flux between nearest neighbor compartments of the submembrane, the bulk myoplasm, and the network SR. This diffusive flux between nearest neighbors i and j has the form $J_d^{ij} = \Delta c_{ij}/\tau_{ij}$, where Δc_{ij} is the concentration difference between the compartments, and τ_{ij} is the diffusion time constant. Since ultrastructural studies of atrial cells show that the distance between junctional and non-junctional CRUs is larger than the distance between non-junctional CRUs, we set the diffusion time between sites on the cell periphery and internal sites to be twice that between internal sites. To set the diffusive time scale between CRUs we rely on our experimental studies which show that subcellular Ca^{2+} waves can travel at a wide range of velocities (4). At 5 Hz pacing we find that wave velocities measured in different atrial myocytes can vary substantially in the range $50\ \mu m/s$ to $200\ \mu m/s$. In this study we have adjusted the subcellular diffusion time scales so that longitudinal planar waves propagate at velocities $100\ \mu m/s - 200\ \mu m/s$ at SR loads in the range $1250\ \mu M - 1400\ \mu M$. All model parameters are given in Table 1 and 2.

Mathematical model of oxidation dependent CaMKII activation: In this study we applied a computational model of CaMKII due to Christensen et al (6), which is based on the model of Dupont et al (7), with modifications to account for oxidative activation. The state diagram of this model is shown in Supplemental figure S9. The states are: I: The inactive CaMKII with occupation probability f_I. B: CaMKII bound to $4Ca^{2+} - CaM$ with probability f_{Bound}. P: Phosphorylated CaMKII with probability f_{Phos}. OxP: Oxidized phosphorylated CaMKII (f_{OxP}) . Ox: Oxidized bound CaMKII (not phosphorylated) with probability f_{Ox}. The equations describing the fraction of bound CaMKII is given by

$$\frac{df_{Bound}}{dt} = k_{IB} \cdot calm \cdot f_I + k_{PB} f_{Phos} + k_{OxB} f_{Ox} - (k_{BI} + k_{BOx} \cdot ROS) f_{Bound} - k_A f_{Bound}$$

where the bound CaM concentration depends on the Ca^{2+} concentration in the submembrane c_s according to

$$calm = \frac{\overline{calm}}{1 + \left(\frac{c_{th}}{c_s}\right)^4} ,$$

where c_s denotes the Ca^{2+} concentration in the vicinity of the RyR cluster. Here we take $c_{th} = 20\mu M$ since c_s can go as high as $100\mu M$ during the peak of a Ca^{2+} spark. In this formulation ROS denoted the concentration of H_2O_2 in μM. The main effect of ROS in this computational model is the addition of a pathway to an active CaMKII state. The occupation probability of the phosphorylated state is given by

$$\frac{df_{Phos}}{dt} = k_A f_{Bound} + k_{OxPP} f_{OxP} - (k_{PB} + k_{POxP} ROS) f_{Phos} .$$

Christensen use a phenomenological on rate given by

$$k_A = k_{BI} \cdot \frac{T_{CaMK}}{T_{CaMK} + 0.01851}$$

where

$$T_{CaMK} = \left(\frac{k_{BI}}{k_{IB}}\right)\frac{f_I}{1-f_I} \ .$$

with $f_I = 1 - f_{Bound} - f_{Phos} - f_{Ox} - f_{OxP}$.

The oxidized states are governed by the equations

$$\frac{df_{Ox}}{dt} = k_{BOx} \cdot ROS \cdot f_{Bound} + k_{OxPOx} f_{OxP} - (k_{OxB} + k_A) f_{Ox} \ ,$$

$$\frac{df_{OxP}}{dt} = k_A f_{Ox} + k_{POxP} \cdot ROS \cdot f_{Phos} - (k_{OxPP} + k_{OxPOx}) f_{OxP} \ .$$

Finally, the CaMKII activity is given by

$$CaMKII_{active} = 0.75 f_{Bound} + f_{Phos} + f_{OxP} + 0.5 f_{Ox} \ .$$

RyR phosphorylation mediated by CaMKII: The RyR model is based on a model of Shannon et al (8) with modifications due to Alvarez-Lacalle et al (9). The model, shown in Supplemental figure S10, consists of 4 states with reaction rates that depend on the local dyadic junction Ca^{2+} concentration and JSR load. In this model we have included a JSR load dependence to the opening rate of the RyR channel that is governed by the function $\phi(c_{jsr})$. This function is taken to have the form

$$\phi(c_{jsr}) = \frac{1}{1 + \left(\frac{c_{jsr}^{th}}{c_{jsr}}\right)^2},$$

where c_{jsr}^{th} is a threshold set by the Ca^{2+} dependence of RyR luminal gating. All constant parameters are given in Table III. In order to model CaMKII phosphorylation we follow Hashambhoy et al (10) and let each RyR state transition between an unphosphorylated and phosphorylated state. Thus, the RyR model consists of 8 states which account for both CaMKII bound and unbound. The transition rate from each unbound state to bound state is taken to have the form $k_{phosp} \cdot CaMKII_{active}$, and with a dephosphorylating rate given by $k_{dephosp}$. In this study we found it necessary to increase the phosphorylation rate parameter of Hashambhoy by a factor of 10 in order to detect appreciable changes in the channel occupation probabilities. Thus, we use rates $k_{phosp} = 0.00238ms^{-1}$ and $k_{dephosp} = 0.000952ms^{-1}$. Following Hashambhoy the closed to open transition rate of phosphorylated RyR is increased by a factor of $Ca_{shift} = 1.5$. Thus, increases in CaMKII will promote RyR phosphorylation which will lead to higher open probability.

Model Parameters:

1. Diffusion Parameters

Parameters of the Restrepo computational cell model. All model parameters not listed below are the same as in the original model (2, 3).

Table 1. Diffusion time constants linking internal sites.

Parameter	**Description**	**Value**
τ_i^T	Transverse cytosolic diffusion time	$1.47ms$
τ_i^L	Longitudinal cytosolic diffusion time	$1.16ms$
τ_s^T	Transverse submembrane diffusion time	$0.71ms$
τ_s^L	Longitudinal submembrane diffusion time	$0.85ms$
τ_{N-SR}^T	Transverse N-SR diffusion time	$3.60ms$

τ_{N-SR}^{L}	Longitudinal N-SR diffusion time	$12.0 ms$

Table 2. Diffusion time constants linking internal and peripheral sites.

Parameter	**Description**	**Value**
τ_i^T	Transverse cytosolic diffusion time	$2.93 ms$
τ_i^L	Longitudinal cytosolic diffusion time	$2.32 ms$
τ_s^T	Transverse submembrane diffusion time	$1.42 ms$
τ_s^L	Longitudinal submembrane diffusion time	$1.7 ms$
τ_{N-SR}^{T}	Transverse N-SR diffusion time	$7.2 ms$
τ_{N-SR}^{L}	Longitudinal N-SR diffusion time	$24.0 ms$

Table 3. RyR parameters.

Parameter	**Description**	**Value**
N	Number of channels in RyR cluster	100
γ	Exponent of Ca^{2+} binding	2.5
c_{th}	Threshold for luminal gating	$400 \mu M$
k_{co}	RyR opening rate parameter	$1.5 \times 10^{-4} (\mu M)^{-2} ms^{-1}$
k_{oc}	RyR closing rate	$1\ ms^{-1}$

k_{oi}	O to I_1 transition rate parameter	$2.0 \times 10^{-4} (\mu M)^{-1} ms^{-1}$
k_{io}	I_1 to O transition rate parameter	$0.02\ ms^{-1}$

Atrial action potential model

For tissue simulations we have applied an atrial AP cell model due to Grandi et al (11), which describes the characteristic triangular AP of atrial myocytes. Important ion current modifications, compared to an established ventricular myocyte model (12), are an 85% reduction of I_{K1}, the absence of $I_{to,slow}$, and shifted activation and inactivation curves for $I_{to,fast}$. Also, an experimentally based ultrarapid delayed rectifier K^+ (I_{Kur}) is incorporated in the model. In this study we have modeled the Ca cycling system using the model of Mahajan et al (13), which accounts for the spatial distribution of Ca release using a phenomenological approach. Although this Ca cycling model was developed for the rabbit myocyte we find that the main features of Ca release and uptake are consistent with our experimental observations of Ca cycling in the dog myocyte. Given that this model is used only to describe electrical wave propagation in tissue, this level of modeling of the Ca cycling system is adequate to address the specific questions at hand.

SUPPLEMENTAL REFERENCES

1. Lammers WJ, Schalij MJ, Kirchhof CJ, and Allessie MA. Quantification of spatial inhomogeneity in conduction and initiation of reentrant atrial arrhythmias. *Am J Physiol.* 1990;259(4 Pt 2):H1254-63.
2. Restrepo JG, Weiss JN, and Karma A. Calsequestrin-mediated mechanism for cellular calcium transient alternans. *Biophys J.* 2008;95(8):3767-89.
3. Restrepo JG, and Karma A. Spatiotemporal intracellular calcium dynamics during cardiac alternans. *Chaos*. 2009;19(3):037115.
4. Aistrup GL, Arora R, Grubb S, Yoo S, Toren B, Kumar M, et al. Triggered intracellular calcium waves in dog and human left atrial myocytes from normal and failing hearts. *Cardiovasc Res.* 2017;113(13):1688-99.
5. Shiferaw Y, Aistrup GL, and Wasserstrom JA. Mechanism for Triggered Waves in Atrial Myocytes. *Biophys J.* 2017;113(3):656-70.
6. Christensen MD, Dun W, Boyden PA, Anderson ME, Mohler PJ, and Hund TJ. Oxidized calmodulin kinase II regulates conduction following myocardial infarction: a computational analysis. *PLoS Comput Biol.* 2009;5(12):e1000583.
7. Dupont G, Houart G, and De Koninck P. Sensitivity of CaM kinase II to the frequency of Ca2+ oscillations: a simple model. *Cell Calcium.* 2003;34(6):485-97.
8. Shannon TR, Wang F, Puglisi J, Weber C, and Bers DM. A mathematical treatment of integrated Ca dynamics within the ventricular myocyte. *Biophys J.* 2004;87(5):3351-71.

9. Alvarez-Lacalle E, Cantalapiedra IR, Penaranda A, Cinca J, Hove-Madsen L, and Echebarria B. Dependency of calcium alternans on ryanodine receptor refractoriness. *PLoS One.* 2013;8(2):e55042.

10. Hashambhoy YL, Greenstein JL, and Winslow RL. Role of CaMKII in RyR leak, EC coupling and action potential duration: a computational model. *J Mol Cell Cardiol.* 2010;49(4):617-24.

11. Grandi E, Pandit SV, Voigt N, Workman AJ, Dobrev D, Jalife J, et al. Human atrial action potential and Ca2+ model: sinus rhythm and chronic atrial fibrillation. *Circ Res.* 2011;109(9):1055-66.

12. Grandi E, Pasqualini FS, and Bers DM. A novel computational model of the human ventricular action potential and Ca transient. *J Mol Cell Cardiol.* 2010;48(1):112-21.

13. Mahajan A, Shiferaw Y, Sato D, Baher A, Olcese R, Xie LH, et al. A rabbit ventricular action potential model replicating cardiac dynamics at rapid heart rates. *Biophys J.* 2008;94(2):392-410.